Manuscript prepared for Atmos. Chem. Phys.
with version 2014/09/16 7.15 Copernicus papers of the LaTeX class copernicus.cls.
Date: 19 May 2016

Spectral Optical Layer Properties of Cirrus from Collocated Airborne Measurements and Simulations

Fanny Finger[1,5], Frank Werner[1,2], Marcus Klingebiel[3], André Ehrlich[1], Evelyn Jäkel[1], Matthias Voigt[3], Stephan Borrmann[3,4], Peter Spichtinger[3], and Manfred Wendisch[1]

[1]Leipzig Institute for Meteorology (LIM), University of Leipzig, Germany
[2]University of Maryland (UMBC), Physics Department, Baltimore, Maryland, USA
[3]Institute for Atmospheric Physics, Johannes Gutenberg University Mainz, Germany
[4]Max Planck Institute for Chemistry, Mainz, Germany
[5]Now at Dr. Födisch Umweltmesstechnik AG, Markranstädt, Germany

Correspondence to: F. Finger
f.finger@uni-leipzig.de

Abstract. Spectral upward and downward solar irradiances from vertically collocated measurements above and below a cirrus layer are used to derive cirrus optical layer properties such as spectral transmissivity, absorptivity, reflectivity, and cloud top albedo. The radiation measurements are complemented by in–situ cirrus crystal size distribution measurements and radiative transfer simulations based on the microphysical data. The close collocation of the radiative and microphysical measurements, above, beneath and inside the cirrus, is accomplished by using a research aircraft (Learjet 35A) in tandem with the towed sensor platform AIRTOSS (AIRcraft TOwed Sensor Shuttle). AIRTOSS can be released from and retracted back to the research aircraft by means of a cable up to a distance of 4 km. Data was collected from two field campaigns over the North Sea and the Baltic Sea in spring and late summer 2013. One measurement flight over the North Sea proved to be exemplary, and as such the results are used to illustrate the benefits of collocated sampling. The radiative transfer simulations were applied to quantify the impact of cloud particle properties such as crystal shape, effective radius r_{eff}, and optical thickness τ on cirrus spectral optical layer properties. Furthermore, the radiative effects of low–level, liquid water (warm) clouds as frequently observed beneath the cirrus are evaluated. They may cause changes in the radiative forcing of the cirrus by a factor of 2. When low–level clouds below the cirrus are not taken into account the radiative cooling effect (caused by reflection of solar radiation) due to the cirrus in the solar (shortwave) spectral range is significantly overestimated.

1 Introduction

Significant uncertainties in atmospheric and climate modelling originate from the insufficient description of effects and interactions of clouds with solar and terrestrial radiation (IPCC, 2013). In particular, cirrus clouds are critical; they mostly warm but can also cool the atmosphere, depending on their optical layer properties (reflectivity, transmissivity, and absorptivity) (Lynch et al., 2002). Cirrus clouds globally occur at various latitudes and in all seasons with a mean global coverage of about 20 – 30 %. More than 70 % of cirrus are observed in the tropics (Wylie et al., 1994), forming relatively stable and long–lived cloud layers (Liou, 1986). Due to different meteorological conditions and evolution processes, cirrus layers are characterized by a wide diversity of macrophysical appearances, as well as ice particles varying in size and number, crystal shapes and orientation. Common horizontal and vertical inhomogeneities of these properties increase the complexity of cirrus. The optical layer properties of cirrus depend mainly on their microphysical ice crystal characteristics such as effective radius (r_{eff}) and ice water content (IWC)

Cirrus inhomogeneities and varying crystal shapes impact (i) the energy budget of the Earth's atmosphere, and (ii) the remote sensing of cirrus optical thickness τ and r_{eff}. The simulations involved in both fields (energy budget and remote sensing) are usually based on one–dimensional (1D) radiative transfer modelling, although significant three–dimensional (3D) effects on solar radiation have been reported. For example, Schlimme et al. (2005) found that the horizontal variability of the extinction coefficient leads to significant differences in the solar irradiance fields below and above the cloud as simulated by 1D and 3D radiative transfer models, which results in a variability of transmittance of about 80 %. Zhang et al. (1999) reported that the net (solar plus terrestrial) radiative forcing of cirrus may switch sign depending on the habits and sizes of the ice crystals of the cirrus. The impact of ice crystal shape on the cirrus radiative forcing, depending on the solar zenith angle, can vary between 10 and 26 % for the solar spectral range (Wendisch et al., 2005), while for the thermal infrared spectral range even larger relative differences of up to 70 % are found (Wendisch et al., 2007). Eichler et al. (2009) investigated the influence of ice crystal shape on the retrieval of τ and r_{eff} and reported effects of up to 70 % for τ and 20 % for r_{eff}.

Measurements of the spectral optical layer properties of cirrus are rarely available. Commonly, a combination of measurements and simulations is applied to derive the optical layer properties, whereby τ and r_{eff} are retrieved from reflected radiance (airborne or spaceborne) (see Francis et al., 1998) and then used in combination with a radiative transfer model to simulate layer reflectivity, transmissivity, and absorptivity.

Airborne measurements of cirrus optical layer properties are hard to obtain if only one aircraft is used, which cannot perform simultaneous measurements of irradiance above and below the cirrus as required to derive the optical layer properties. Usually, the radiative measurements above and below the cirrus are performed consecutively (e.g., Pilewskie and Valero, 1992), or using two aircrafts, one below and the other one above the cirrus. Both methods unavoidably involve temporal shifts be-

tween the two measurements above and below the cirrus and, thus, can be applied for rather static and horizontal homogeneous cloud layers only. Therefore, helicopter–borne towed platforms have been developed and adapted, such as the Airborne Cloud Turbulence Observation System (ACTOS) for microphysical in situ instruments, and the Spectral Modular Airborne Radiation measurements sys-
60 Tem – HELIcopter–borne Observations of Spectral Radiation (SMART–HELIOS) for solar spectral reflectivity measurements (Henrich et al., 2010; Werner et al., 2013, 2014). For cirrus measurements, Frey et al. (2009) introduced the aircraft–borne AIRTOSS (AIRcraft TOwed Sensor Shuttle), shown in Fig. 1, which enabled one to perform collocated radiation measurements above and microphysical measurements above and within the cirrus, to compare the remote sensing of crystal microphysical
65 properties with in situ data. Frey et al. (2009), however, did not allow for collocated radiation measurements above and below cirrus because the radiation sensors were only installed on the aircraft. In this paper we demonstrate a significantly improved sensor setup with radiation measurements on both the aircraft and the towed sensor platform (AIRTOSS) allowing for truly collocated radiation measurements to be conducted for the first time. In Section 2 the instrumentation of the aircraft and
70 of the extended setup of AIRTOSS is described. In particular, the solar spectral radiation instruments and their unique combination to deduce cirrus optical layer properties are discussed in Section 3. In Section 4 the calculated solar spectral layer properties of cirrus and the concurrent microphysical observations are introduced for one exemplary measurement case. Based on the data radiative transfer simulations are performed and analyzed in Section 5.

75 ## 2 Instrumentation

The instruments were mounted at three different positions: on the aircraft (Section 2.1), an additional wing pod underneath the left wing (Section 2.1), and the towed platform AIRTOSS (Section 2.2) as illustrated in Fig. 2 (a). The operation of the aircraft together with the tethered AIRTOSS is certified for altitudes up to 12.5 km (the previous ceiling limitation was 7.6 km; Frey et al., 2009).

80 ### 2.1 Aircraft

The aircraft certified for the operation of AIRTOSS is a Learjet 35A. Instruments for measurements of trace gases and water vapor are mounted inside the cabin with special inlets sampling ambient air from outside the aircraft during the flight. The analysis of the collected trace gas data is published elsewhere (Mueller et al., 2015). An upward looking radiation sensor, measuring the downward
85 spectral irradiance $F^{\downarrow}$ (in $\mathrm{W\,m^{-2}\,nm^{-1}}$), was mounted on the fuselage including the Spectral Modular Airborne Radiation measurement syStem (SMART) inside the aircraft, introduced by Wendisch et al. (2001), and further developed by Bierwirth et al. (2009). Optical fibers connect the optical inlet with two Zeiss spectrometers for the visible to near–infrared (300 – 2200 nm) wavelength range with a resolution (Full Width at Half Maximum, FWHM) of 2 – 3 nm (visible) and 9 – 16 nm (near–

infrared), respectively. An active horizontal stabilization platform (Wendisch et al., 2001) was operated to assure the horizontal levelling of the upward looking optical inlet on top of the aircraft during the aircraft measurements. A pod mounted under the left wing of the aircraft contains another optical inlet with a pair of spectrometers, measuring the upward spectral irradiance $F^{\uparrow}$. A Forward Scattering Spectrometer Probe (FSSP–100), placed at the tip of the wing pod, measures the cloud particle number size distribution (size diameter range from 2 to 47 µm, Gayet et al., 2002). To correct for shattering (Korolev et al., 2013) the FSSP–100 records the individual data particle–by–particle (Field et al., 2003, 2006). The instrument clearly indicated the time periods when the aircraft was inside clouds.

2.2 AIRTOSS

AIRTOSS, as shown in Fig. 2 (b), has a length of 2.85 m and a diameter of 24 cm; the maximum payload is 40 kg. AIRTOSS can be released from and retracted to the aircraft by a 4 km long towing cable.

In the front part of AIRTOSS in flight direction the Cloud Combination Probe (CCP, see e.g., Wendisch and Brenguier, 2013; Klingebiel et al., 2015) is installed. The CCP consists of the Cloud Droplet Probe (CDP) and the Cloud Imaging Probe instrument (CIP grey scale – denoted as CIPgs in the following). The CDP measurement principle is similar to the FSSP–100; it detects particles in the size diameter range between 2 µm and 50 µm by measuring the forward–scattered light of a laser beam which hits the ice crystals in the cirrus. The CIPgs records two–dimensional (2D) shadow images of the cirrus particles and covers a size range between 15 µm and 960 µm with an optical resolution of 15 µm. The performance of these microphysical cloud probes in cirrus clouds was characterized by McFarquhar et al. (2007).

The center part of AIRTOSS contains a battery for power supply, which is sufficient to assure electrical power for measurements of about two hours. The radiation setup is mounted in the backward part of AIRTOSS. It consists of two spectrometer pairs and two optical inlets, one upward– and one downward–looking, measuring the downward and upward spectral irradiances $F^{\downarrow}$ and $F^{\uparrow}$. Additional sensors for static air temperature and relative humidity, latitude, longitude and position angles pitch, roll and heading of AIRTOSS are installed.

The housing of the towed platform consists of an aerodynamic canister to avoid irregular movements and to enable stable flights, which is crucial for reliable radiation measurements (Frey et al., 2009).

3 Cirrus optical layer properties

Four optical inlets, two for upward and two for downward irradiance measurements were mounted on the Learjet 35A and AIRTOSS. This setup enabled simultaneous measurements of the irradiance in two different altitudes (e.g., above and below cloud) as required for the derivation of cirrus optical

layer properties (see Fig. 3). By measuring the upward and downward irradiances at the top and base of a cloud layer the optical properties are derived by the following equations. The reflectivity R is given by:

$$R = \frac{F^{\uparrow}_{\text{top}} - F^{\uparrow}_{\text{base}}}{F^{\downarrow}_{\text{top}}}. \tag{1}$$

R quantifies the relative portion of incoming solar radiation that is reflected by the cloud layer. The transmissivity T of a cloud layer is defined by:

$$T = \frac{F^{\downarrow}_{\text{base}}}{F^{\downarrow}_{\text{top}}}. \tag{2}$$

T describes the part of the incoming irradiance transmitted through the cloud. The relative portion of irradiance absorbed inside the cloud layer is defined by the absorptivity:

$$A = \frac{(F^{\downarrow}_{\text{top}} - F^{\uparrow}_{\text{top}}) - (F^{\downarrow}_{\text{base}} - F^{\uparrow}_{\text{base}})}{F^{\downarrow}_{\text{top}}}. \tag{3}$$

Equation 3 implicitly assumes that there are no horizontal components of radiative flux divergence, only vertical flux divergences are considered to derive absorptivity by Eq. 3. From these definitions it follows:

$$R + T + A = \frac{F^{\uparrow}_{\text{top}} - F^{\uparrow}_{\text{base}} + F^{\downarrow}_{\text{base}} + F^{\downarrow}_{\text{top}} - F^{\uparrow}_{\text{top}} - F^{\downarrow}_{\text{base}} + F^{\uparrow}_{\text{base}}}{F^{\downarrow}_{\text{top}}} = 1. \tag{4}$$

In addition to the three optical layer properties defined by Eqs. 1–3, the cloud top albedo R_{top} is given by:

$$R_{\text{top}} = \frac{F^{\uparrow}_{\text{top}}}{F^{\downarrow}_{\text{top}}}. \tag{5}$$

R_{top} describes the cloud reflection property of the cloud layers and the underlying surface. For investigating the effect of a cirrus layer on the atmospheric radiative energy budget the radiative forcing (RF_{toa}) at the top of atmosphere (toa) is used, which is defined by:

$$RF_{\text{toa}} = (F^{\downarrow}_{\text{toa}} - F^{\uparrow}_{\text{toa}})_{\text{cloud}} - (F^{\downarrow}_{\text{toa}} - F^{\uparrow}_{\text{toa}})_{\text{clear sky}}. \tag{6}$$

The subscripts "cloud" and "clear sky" indicate measurements or simulations in cloudy conditions and in a clear sky (i.e., an atmosphere containing no clouds) atmosphere. Following Eq. 6, RF_{toa} is the net of solar (shortwave) and terrestrial (longwave) radiation for the atmospheric conditions. A positive RF_{toa} indicates a net warming effect of the cloud by absorbing outgoing energy from the Earth's surface. A negative RF_{toa} indicates a net cooling effect mainly due to reflecting of incoming solar radiation. The following investigations are focused on the solar spectrum from 300 nm to 2300 nm.

4 Observations

Measurements were performed during two observational campaigns in spring (6 – 8 May) and late summer (29 August – 5 September) in 2013. The research flights were based at the military airports in Hohn and Jagel, North Germany, and were carried out in restricted flight areas above the North and Baltic Sea. The measurement areas represent rectangles with the size of 50 x 80 km^2, and 35 x 80 km^2, respectively. Stepwise horizontal flight patterns were flown to collect radiative and microphysical data at different altitudes (6 – 11.5 km). In total, twelve measurement flights were carried out during both campaigns.

Measurements are presented of one exemplary flight which took place west of the German island of Helgoland above the North Sea (54.98° – 54.43°N, 6.59° – 7.57°E); it was performed on 30 August 2013 (08:33 – 09:48 UTC). Northern Germany was under the influence of an occluded front with associated cirrus and the center of the low situated south of Norway (see Fig. 4).

Fig. 4 (a) shows the corresponding composite satellite image of METEOSAT–10. In the image the cirrus is indicated by the color white. Low–level water clouds, indicated by the color yellow, are widespread and cover parts of the measurement areas. The flight track of the Learjet 35A is shown in Fig. 4 (b).

4.1 Microphysical measurements

Fig. 5 shows the vertical profiles of (a) static air temperature (in °C), (b) relative humidity (in %) with respect to ice, measured by instruments on the aircraft, (c) number concentration (in cm^{-3}), and (d) mean diameter (in µm), measured by the CIPgs on AIRTOSS. The bars quantify the measurement errors, resulting from instrument uncertainties (a, b), counting statistics (c), and determination of the depth of field (d). From measured ice particle number concentrations, cirrus was identified in two layers between the altitude of 6.7 km and 8.5 km and between 9.0 km and 9.2 km, with a temperature range of $-21\,°C$ to $-39\,°C$.

Fig. 5 (c) and (d) show the particle number concentration and mean diameter as a function of altitude. Each data point represents a mean value for a 200 m height interval. The cirrus layer between 6.7 and 8.5 km is characterized by values for the ice crystal number concentration of 1.2 x 10^{-4} cm^{-3} to 2.1 x 10^{-3} cm^{-3} and for the crystal mean diameter of 146 and 178 μm, representing an optically thin and vertically well mixed cirrus. The gaps of measured number concentration and mean diameter are due to measurements outside the observed cirrus. The second cirrus layer between 9.0 and 9.2 km altitude shows increased values for the crystal number concentration of up to 7.9 x 10^{-3} cm^{-3} and lower values for the crystal mean diameter of 33.5 to 87.4 μm. This results in an increasing optical thickness of the upper cirrus layer in comparison to the underlying cirrus layer assuming a comparable vertical extent of 200 m.

4.2 Radiation data

4.2.1 Spectral irradiances

In Fig. 6 (a) the time series of downward and upward irradiance measured by the spectrometers on AIRTOSS at an exemplary wavelength of 550 nm is illustrated for the entire flight: gray for downward and light blue for upward irradiance. The altitude of the Learjet (dashed red line in Fig. 6 (b)) and AIRTOSS (solid red line) show the stepwise climbing flight pattern and the different altitudes of the level legs as well as the vertical distance of about 200 m between both. The gray colored peaks in the time series of the irradiance (Fig. 6 (a)) are due to flight manoeuvers and should be excluded from further analysis. The measured pitch and roll angles of the AIRTOSS were used to sort out the data with nearly horizontal orientation, which is crucial for irradiance measurements (Wendisch et al., 2001). Here a threshold of 5° was assumed in order for the data to be accepted. As a result the thickened line periods mark the measuring points with suitable flight legs during which the levelling of the irradiance sensors was assured. Almost constant values of the downward irradiance (1.09 – 1.20 $\mathrm{W\,m^{-2}\,nm^{-1}}$) are recorded within these time periods. The upward irradiance is influenced by the surface albedo and changing conditions due to underlying clouds; they show values between 0.56 and 0.81 $\mathrm{W\,m^{-2}\,nm^{-1}}$ at the wavelength of 550 nm.

As the AIRTOSS is towed beneath the aircraft, a horizontal displacement between the measurements on the Learjet and on the AIRTOSS needs to be accounted for. Therefore, a temporal shift of the radiation measurements on the towed platform and that measured on the Learjet 35A has to be considered to guarantee clear vertical collocation of the measurements. The temporal shift between the aircraft and AIRTOSS was calculated by using the cable length (914 m), aircraft velocity (150 – 170 $\mathrm{ms^{-1}}$) and altitude difference of both platforms, as a function of the true air speed. The resulting altitude and time difference varies between 160 m and 210 m, corresponding to 4.8 seconds to 6 seconds time shift.

Mean values of measured spectra of upward and downward irradiance from both platforms are shown in Fig. 7 from the time interval indicated by the dashed lines in Fig. 6. The investigated cirrus layer is located between 9 and 9.2 km altitude and can be seen in Fig.5 (c) and (d), indicated by the upper gray colored layer. This measurement example was chosen due to the higher optical thickness, as reported in Section 4.1, and because of the low vertical extent, which enables to measure above and below this cirrus layer. Additionally, a second cirrus layer is located between 6.7 km and 8.5 km altitude overlying a low–level water cloud between about 1 km and 1.25 km altitude.

The vertical difference between the two measurement platforms is 195 m in the specific example discussed here. The downward irradiance $F^{\downarrow}_{\mathrm{top}}$ at the top of the cloud layer was simulated using libRadtran (Mayer and Kylling, 2005). The black solid lines in Fig. 7 show the irradiance, measured in the flight altitude of the Learjet above the cloud layer (subscript top), the black dotted lines represent the irradiance measured from the AIRTOSS at the base of the investigated part of the cirrus

layer (subscript base).

As expected, the downward irradiance below the cirrus ($F^{\downarrow}_{\text{base}}$) is lower than that measured above the cloud ($F^{\downarrow}_{\text{top}}$). This shows that the attenuation of the solar radiation (reflection and absorption by cirrus particles) by the observed cirrus can actually be quantified by observational means. The upward irradiances ($F^{\uparrow}_{\text{top}}$ and $F^{\uparrow}_{\text{base}}$) are relatively high. This is due to underlying low–level clouds below the cirrus within the measurement area during the selected measurement period. The lower upward irradiance was also measured for an atmosphere without clouds between the cirrus and ocean surface (dashed line in Fig. 3)

Due to the high flight altitude, about 9.2 km, little water vapor absorption can be observed in the near infrared absorption bands as indicated by the almost unaffected downward irradiance in both levels. Therefore, most of the absorption of solar radiation measured in the downward irradiance below the cirrus originates from the cirrus particles itself.

The upward radiation depends on the albedo of the Earth's surface and underlying clouds, as can be seen in enhanced values of upward irradiance. The absorption bands of liquid water, as well as water vapor absorption, at wavelengths of 1140 nm or 1400 nm are obvious in the spectra. Furthermore, the irradiances $F^{\uparrow}$ at both altitudes are almost similar. In comparison to the bright surface the difference due to the cirrus is not significant.

4.2.2 Spectra of reflectivity, absorptivity, transmissivity

By measuring the spectral and collocated upward and downward irradiances at two altitudes the cloud optical layer properties of the cirrus layer are derived according to Eq. (1) – (3).

Fig. 7 (b) shows the spectral transmissivity (red, see Eq. 2), reflectivity (black, see Eq. 1), absorptivity (green, see Eq. 3), and cloud top albedo (gray, see Eq. 5) in the visible and near infrared wavelength range according to the example in Fig. 7 (a). The error bars result from the Gaussian error propagation due to uncertainties of calibration, of deviations from the ideal cosine angular sensor response correction, dark current, and signal to noise ratio. The resulting percentage errors range between 5 % and 6 % with higher values for the near infrared wavelength range.

As cirrus clouds are optically thin, the transmissivity dominates over the entire spectral range with high values between 0.88 and nearly 1. The reflectivity in Fig. 7 (b) shows very low values of less than 0.03. This is due to the optically and vertically thin cirrus layer and a brighter water cloud underneath. The effect of low–level clouds can be seen in the large values of cloud top albedo of approximately 0.4 to 0.6 in the depicted wavelength range.

The transmissivity shows a slightly negative spectral slope, absorptivity a positive trend, and the reflectivity shows no spectral trend. As the imaginary part of the refractive index is associated with the absorption coefficient, which increases with increasing wavelength (for wavelengths longer than approximately 1000 nm), the measured absorptivity shows a spectral trend with a positive slope and values up to 0.12 in the near infrared range. It points out the importance of cirrus clouds in this

wavelength range.

A time series of the cloud optical layer properties (at 1640 nm) is given in Fig. 8, with (a) transmissivity, (b) absorptivity, and (c) reflectivity, for the cirrus layer between 9.0 and 9.2 km altitude and a horizontal distance of 10.4 km. The cloud top albedo from below the aircraft (gray triangles), representing the cirrus and low–level cloud, is plotted in (d).

The right panels (e)–(h) show the histograms for the respective cirrus properties in the left representing the variability during this flight part. As T, A, and R are cloud layer properties, the varying values are due to changing optical and microphysical properties of the cirrus. The layer properties of this thin cirrus show small variations, thus indicating small spatial heterogeneity of the cirrus optical layer properties. The transmissivity reveals the smallest variation between 0.890 and 0.925 (4 %). Absorptivity and reflectivity range between 0.078 and 0.098, and 0.001 – 0.008 resulting in a percentage difference of 21 % and 87 %, respectively. This is still within the error bars as shown in the left panels (b) and (c) of Fig. 8.

The larger variability of R_{top} is explained by the changing reflectivity properties of the surface on the cloud top albedo. As the cirrus layer is optically thin, R_{top} from above the cirrus is strongly affected by the surface albedo and bright underlying water clouds. This results in significant R_{top} variations between 0.35 and 0.39 representing a difference of about 11 %.

5 Sensitivity studies based on radiative transfer simulations

In this section sensitivity studies of the cirrus optical properties using radiative transfer simulations are presented. In the following section the one–dimensional radiative transfer model is introduced. It is applied for individual cirrus layers as well as for atmospheric cases including a cirrus and an underlying low–level cloud.

5.1 Model introduction

To compare the measurements with simulations and for a measurement–based quantification of the impact of different parameters, such as cloud particle shape and size on cirrus cloud optical layer properties, sensitivity studies with the one–dimensional (1D) radiative transfer model libRadtran (Mayer and Kylling, 2005) are performed. Included is the DISORT (DIScrete Ordinate Radiative Transfer) code by Stamnes et al. (2000). The observed cirrus layer is represented by varying cloud properties. The corresponding upward and downward irradiances at the top and the base of the cirrus are calculated to obtain the optical layer properties reflectivity, absorptivity, and transmissivity (according to Eq. (1) – (3)), and the cloud top albedo and radiative forcing (Eq. (5) and (6)).

The required volumetric extinction coefficient $\langle b_{\text{ext},\lambda} \rangle$, single–scattering albedo $\langle \omega_\lambda \rangle$, and phase function $\langle p_\lambda \rangle$ are derived by combining calculated tables of single scattering properties by Yang et al. (2005) with a specific in situ measured number size distribution $\mathrm{d}N\,/\,\mathrm{d}D$ (in cm^{-3}) from the

CCP installed on AIRTOSS. The single scattering properties for individual particles (extinction coefficient $C_{\text{ext},\lambda}$, scattering coefficient $C_{\text{sca},\lambda}$, single–scattering albedo ω_λ, and phase function p_λ) with different particle radii are weighted with the number size distribution. The resulting spectral volumetric properties are used as input parameters for the radiative transfer simulations. The spectral volumetric extinction coefficient $\langle \text{b}_{\text{ext},\lambda} \rangle$ in units of km^{-1} was obtained by (see Wendisch et al., 2005):

$$\langle b_{\text{ext},\lambda} \rangle = \int C_{\text{ext},\lambda} \cdot \frac{dN}{dD} \cdot dD. \tag{7}$$

The boundaries of integration are defined by the size diameter range of the CCP. A similar algorithm was used to derive the spectral volumetric single–scattering albedo $\langle \omega_\lambda \rangle$ by calculating:

$$\langle \omega_\lambda \rangle = \frac{\int \omega_\lambda \cdot C_{\text{ext},\lambda} \cdot \frac{dN}{dD} \cdot dD}{\langle b_{\text{ext},\lambda} \rangle}. \tag{8}$$

Furthermore, the volumetric phase function $\langle p_\lambda \rangle$ is obtained by:

$$\langle p_\lambda \rangle = \frac{\int p \cdot C_{\text{sca},\lambda} \cdot \frac{dN}{dD} \cdot dD}{\int C_{\text{sca},\lambda} \cdot \frac{dN}{dD} \cdot dD}. \tag{9}$$

5.2 Individual cirrus layer

To compare, in a first step, the measured cloud optical layer properties R, T, A, and cloud top albedo R_{top} with the simulated quantities, Fig. 10 (a) – (e) shows simulations of a cirrus layer between 9.0 and 9.2 km altitude with different optical thicknesses. The input for the simulations includes a measured number size distribution, shown in Fig. 9, which was measured during the AIRTOSS campaign and represents a typical cirrus. The composition of ice crystal shapes is assumed to be constant, further assuming a mixture of particle shapes according to Baum et al. (2005).

The cirrus optical thickness varies between 0.11 and 0.55. As expected, an increasing optical thickness leads to a decreased transmissivity T and increased reflectivity R, absorptivity A, and cloud top albedo R_{top}. The spectral trend shows pronounced effects for T and A in the near infrared wavelength range excluding the ranges of the water vapor absorption bands resulting in percentage differences of 8 % (0.91 – 0.98) and a factor of 5 (0.01 – 0.05), respectively, between the optically thinnest and thickest cloud layer. The absorptivity varies in the range of the ice particle absorption and causes a difference by up to a factor of 5, similarly the cloud top albedo shows a difference of a factor of 5 (0.007 – 0.038) in the wavelength range of water vapor absorption. R reveals the same absolute values and resulting percentage differences in the addressed wavelength range as well as in the complete wavelength range, which was investigated here. According to the changes in the layer properties, the radiative forcing varies most between those cases while the absolute differences are small, varying between -0.006 ($\tau = 0.11$) and -0.033 $\text{W m}^{-2}\,\text{nm}^{-1}$ ($\tau = 0.55$, at 550 nm).

Comparing the measured (diamonds) and simulated (lines, in Fig. 10) spectral cloud optical layer properties, it can be seen, that there are obvious discrepancies due to different variable input parameters such as optical thickness, ice crystal shape, and properties of the underlying surface.

As a cirrus cloud of 200 m vertical extent is not a typical one, for further sensitivity studies a cirrus between 6.7 and 8.5 km altitude is assumed, according to the measurement case of 30 August 2013 (see Fig. 5). The implemented number size distribution (Fig. 9) and the assumption of a mixture of shapes, described by Baum et al. (2005), results in a cirrus optical thickness of 1, representing a typical cirrus cloud, see Sassen and Comstock (2001) ($\tau_{\mathrm{Ci}} = 0.03 - 1.66$) and Platt et al. (1980) ($\tau_{\mathrm{Ci}} = 0.5 - 3.5$).

To investigate the effect of different ice crystal shapes (see Fig. 11), a fixed number size distribution is combined with different shape assumptions: Solid Column, Column – 8 Elements, Plate, Plate – 10 Elements, Solid Bullet Rosette, Droxtal, and a mixture of 30 % Plates (10 Elements), 30 % Hollow Bullet Rosettes, 20 % Plates, and 20 % Hollow Columns, similar to the mixture according to Baum et al. (2005). The multi–component ice crystals, such as Column – 8 Elements, are aggregates consisting of their respective number of crystals. The different crystal shapes are introduced by Yang et al. (2013). The ice crystal roughness is set to smooth, see Baum et al. (2010).

Two approaches are investigated: (I) the number size distribution is constant (NSD, left panels), (II) the ice water content is constant (IWC, right panels). While the number size distribution is derived from in situ measurements, assuming a constant IWC for a cirrus layer under constant atmospheric conditions is a more physical approach.

Fig. 11 shows the simulated (lines) spectral optical layer properties transmissivity T (a,e), reflectivity R (b,f), and absorptivity A (c,g) for those crystal shapes. Additionally, the simulated radiative forcing RF_{toa} (see Eq. 6) in (e,h) are represented. As reference case the shape Droxtal (red line) is used approximating spherical particles. Table 1 shows the resulting optical thicknesses and effective radii assuming different shapes for the two approaches.

The results for approach I show, that varying ice crystal shape causes differences that are spectrally dependent, especially for absorptivity in the near infrared wavelength range between 1450 and 1800 nm, and 1900 and 2200 nm, where the imaginary part of the refractive index of ice reveals a maximum. This corresponds to an increased absorption coefficient and, therefore, a pronounced shape effect in this wavelength range. A similar behavior can be seen in the spectral trend of the transmissivity.

The percentage difference of transmissivity between the varying shapes and the reference case (Droxtals, 0.57 at 2000 nm) ranges between 2 % and 48 %. The lowest differences show Solid Columns (0.56) and Plates, whereas the mixture according to Baum et al. (2005) and Plates (10 Elements) show highest values (0.84). The shape variability is more pronounced for reflectivity and absorptivity with differences of up to a factor of 3 (0.023 – 0.078) and a factor of 2 (0.04 – 0.29) for Plates (10 Elements), respectively.

In relation to the highest values of reflectivity the corresponding radiative forcing for Solid Columns and Droxtals are strongest with -0.20 and -0.18 $\mathrm{W\,m^{-2}\,nm^{-1}}$ (at 550 nm), and for Plates (10 Elements) and the mixture according to Baum et al. (2005) lowest with -0.05 and -0.06 $\mathrm{W\,m^{-2}\,nm^{-1}}$

(550 nm), respectively. It results in a pronounced cooling effect for Droxtals and Solid Columns, according to the highest values of optical thickness, while the effective radius is constant (see Table 1). This leads to a difference in the radiative forcing of a factor of up to 4 assuming different shapes. Assuming a constant IWC of 0.395 g m^{-3} (approach II) for varying ice crystal shapes means keeping the total volume of the cirrus cloud particles constant. It causes a shift in the number size distribution and a changing r_{eff}. The reference value for the IWC is derived by assuming spherical cloud particles. This leads to the largest variabilities between Droxtals, approximating spheres, and crystal shapes with a large surface area, such as aggregates of shapes or Rosettes. For transmissivity (0.16 – 0.40, at 2000 nm) and absorptivity (0.38 – 0.44) the resulting differences are smaller than 60 %. The largest differences are obtained for the reflectivity (0.10 – 0.40, factor of 4) as well as for radiative forcing (-0.25 to -0.52 W m^{-2} nm^{-1}, at 550 nm) by a factor of 2, due to the link between the total surface area of a cloud and its capability of reflection. This can be seen in the inverse relation between τ and r_{eff} in Table 1, as well. In comparison with approach I the second scenario II shows significantly larger variabilities assuming different shapes for the cloud optical layer properties and radiative forcing.

5.3 Cirrus and underlying low–level cloud

Chang and Li (2005) reported an annual and global occurrence of high clouds of 52 -- 61 % (ocean – land), from which 27 % to 29 % represent cases with low clouds underneath the cirrus. During the flights very often low clouds were observed, that is why the related effect of a low–level water cloud was investigated. Fig. 12 shows two conditions, one with (black line) and one without (red line) a low–level water cloud. The cirrus is the same case as in Fig. 11, Approach I, assuming the mixture of shapes according to Baum et al. (2005). For the second case a water cloud (τ = 20) was added between 1 km and 1.25 km altitude. The measurement example is the same as shown in Fig. 7 (b).
Adding a low–level cloud in the simulations leads to the strongest effects in the visible wavelength range with a higher transmissivity (0.94 to 0.99, difference of 5 %) and lower reflectivity (0.06 to 0.01, up to 85 % difference) of the cirrus layer except in the wavelength ranges of the water vapor absorption bands. The absorptivity differs rarely. A difference can be seen in the wavelength range of about 2000 nm with the largest absolute difference of 0.114 (Cirrus) to 0.134 (Cirrus + low water cloud), resulting in a percentage difference of 15 %. As the cloud top albedo is no cirrus layer property it shows the largest difference for the low–level cloud case, but is in good agreement with the measurement case in the shortwave–infrared wavelength range.
For characterizing the effect of a low–level water cloud on the radiative forcing of the cirrus and the atmosphere's energy budget, a modified radiative forcing RF'_{Ci} is introduced:

$$RF'_{\text{Ci}} = RF_{\text{Ci+low cloud}} - RF_{\text{low cloud}} \qquad (10)$$
$$RF'_{\text{Ci}} = F^{\uparrow}_{\text{low cloud}} - F^{\uparrow}_{\text{Ci+low cloud}}.$$

The resulting RF'_{Ci} is the difference between the case of a cirrus with underlying low water cloud and the case with the low cloud only (as Keil and Haywood (2003) applied for aerosol layers) at the top of atmosphere.

RF'_{Ci} is shown in Fig. 12 (e) (black line) in contrast to the radiative forcing RF (see Eq. 6) of the same but single–layer cirrus (red line). This leads to an overestimation of the cooling effect of the cirrus with a percentage difference of about 80 % (-0.05 to -0.01 $\mathrm{W\,m^{-2}\,nm^{-1}}$) in the visible wavelength range and up to a factor of 2 in the near infrared range caused by the low–level cloud. Furthermore, there is a sign changing effect on RF' with negative values for the visible spectral range and a positive radiative forcing in the near infrared range (-0.002 to 0.002 $\mathrm{W\,m^{-2}\,nm^{-1}}$).

The results obtained in this paper are valid for the respective cloud cases. To evaluate the low–level cloud effect on the cirrus the properties of the low water cloud, such as optical thickness and cloud top height, have to be investigated, too. Therefore, Fig. 13 (a) and (b) show values of integrated cirrus radiative forcings (wavelength range: 300–2300 nm) with varying water cloud optical thickness (a) and cloud top height (b). The cirrus is located between 6.7 km and 8.5 km altitude and consists of the mixture of shapes according to Baum et al. (2005). The color code represents the changing cirrus optical thickness.

In Fig.13 (a) the low–level cloud is located between 1 km and 1.25 km with an increasing optical thickness from 5 to 60. In general, the cooling of the cirrus decreases with increasing optical thickness of the low–level cloud resulting in an increasing influence of the low cloud on the radiative forcing of the upper lying cirrus. An increase of radiation reflected by the lower cloud is available to interact with the cirrus compared to single cloud layer conditions. With increasing water cloud optical thickness a saturating effect becomes evident resulting in a difference of 83 % ($32\,\mathrm{W\,m^{-2}}$) for the cirrus with $\tau = 2$ and an absolute difference of the water cloud optical thickness of 55. Additionally, with increasing cirrus optical thickness the absolute difference of RF'_{Ci} increases from $10\,\mathrm{W\,m^{-2}}$ ($\tau_{\mathrm{Ci}} = 0.5$) to $32\,\mathrm{W\,m^{-2}}$ ($\tau_{\mathrm{Ci}} = 2$).

In Fig.13 (b) the low water cloud has a constant optical thickness of 20 and a vertical thickness of 250 m with an increasing cloud top height from 1.25 to 7.25 km in steps of 1 km. Here, the amount of the reflected radiation by the low cloud, available in the cirrus level, depends on the vertical extension of the atmosphere in between and its interaction with the transmitted (from cirrus) and reflected (from water cloud) radiation. Fig.13 (b) shows a decreasing solar cooling with an increasing cloud top height of the low–level cloud. This results in a difference of $8\,\mathrm{W\,m^{-2}}$ ($\tau_{\mathrm{Ci}} = 2$) for a vertical difference of the cloud top height of 6 km. The trend of RF'_{Ci} represents a similar saturating effect with increasing cloud top height resulting in percentage differences of 20 % ($\tau_{\mathrm{Ci}} = 0.5$) to 35 % ($\tau_{\mathrm{Ci}} = 2$). It is noticeable that the effect due to the optical thickness of the low cloud (a) in comparison to the effect of the cloud top height (b) has a stronger influence on the radiative forcing of the above lying cirrus.

6 Conclusions

Solar spectra of optical layer properties of cirrus have been derived from first truly collocated airborne radiation measurements using a Learjet and the improved towed sensor platform AIRTOSS (AIrcraft TOwed Sensor Shuttle). The radiation measurements are complemented by microphysical in–situ measurements and radiative transfer simulations, based on the measured microphysical data. Two field campaigns have taken place above the North Sea and the Baltic Sea in spring and late summer 2013. The aircraft (Learjet 35A) and the towed platform AIRTOSS, released on a towing cable underneath the plane, collected radiation and microphysical data above, beneath and inside the cirrus. For radiation measurements the straight flight legs with minor changes of pitch and roll movements of the measurement platform are selected for detailed analysis.

The spectral upward and downward irradiances in the visible and near infrared wavelength range measured above and below the cirrus have been used to derive the spectral transmissivity, absorptivity, reflectivity, and cloud top albedo of the observed cirrus layer. The irradiance spectra and an exemplary time series for a straight flight leg of 30 August 2013 are analyzed. The resulting layer properties at one wavelength in the near infrared range (1640 nm) differ slightly due to horizontal inhomogeneities and the influence of low–level clouds. An increased effect due to low clouds is observed in the cloud top albedo with varying values between 0.35 to 0.39, resulting in a percentage difference of up to 11 %.

The impact of varying ice crystal shape and cloud particle size distribution is studied applying a 1D radiative transfer model in combination with volumetric extinction coefficient, single–scattering albedo, and phase function calculated from the measured ice crystal number size distributions and tables of ice crystal single–scattering properties. The results show the highest sensitivity in cloud optical layer properties for varying ice crystal shapes for the reflectivity with up to a factor of 3 with respect to the reference case of nearly spherical shaped Droxtals. The respective cirrus radiative forcing differs by a factor of up to 4 with a strong cooling effect for Droxtals. A similar effect is due to an additional low–level water cloud, as observed during the measurement flight, with a noticeable difference in the reflectivity of the cirrus of up to 85 % under multi–layer cloud conditions. The radiative forcing of the cirrus layer may switch sign and shows positive values in the near infrared wavelength range with a resulting difference of up to a factor of 2. It was found that if the low–level cloud is not considered the solar cooling of the cirrus is strongly overestimated. The variation of the low–level cloud properties cloud top height and optical thickness influences the cirrus radiative forcing, too, resulting in differences of 35 % and 83 %, respectively.

The application of measured in situ microphysical properties as input of radiative transfer simulations did not accurately reproduce the measured cirrus optical layer properties. This is partly due to a variety of possible ice crystal shapes and mixtures of shapes, which was not measured, and the impact of a changing albedo during the flight. Because the low–level water cloud has a significant influence, more information of the water cloud is needed as well. Further adjustment of the simula-

tions can probably be used to optimize the agreement and derive more information on the particle properties. The effect of the low–level water cloud has to be further investigated by varying the properties of the cirrus, such as shape, size, and height of the cloud base and top. As the interaction of the cirrus with terrestrial radiation is an important factor for affecting the Earth's energy budget, radiative transfer calculations in the terrestrial wavelength range have to be investigated in future data analysis of the field measurements.

Acknowledgements. This study was supported by the Deutsche Forschungsgemeinschaft through Project "WE 1900/19–1, BO 1829/7–1". Additional funding on a similar level for the aircraft certification of AIRTOSS and for conducting the campaign was provided by internal sources of the Particle Chemistry Department at the Max Planck Institute for Chemistry. We thank the pilots and crew of the Gesellschaft für Flugzieldarstellung (GFD) and enviscope GmbH for preparation and execution of the test and research flights, and the colleagues from Forschungszentrum Jülich and University of Warsaw for their support.

References

Baum, B. A., Yang, P., Heymsfield, A. J., Platnick, S., King, M. D., Hu, Y. X., and Bedka, S. T.: Bulk scattering properties for the remote sensing of ice clouds. Part II: Narrowband models, J. Appl. Meteor., 44, 1896–1911, 2005.

Baum, B. A., Yang, P., Hu, Y. X., and Feng, Q. A.: The impact of ice particle roughness on the scattering phase matrix RID B-7670-2011 RID B-4590-2011, J. Quant. Spectrosc. Radiat. Transfer, 111, 2534–2549, doi:10.1016/j.jqsrt.2010.07.008, 2010.

Bierwirth, E., Wendisch, M., Ehrlich, A., Heese, B., Tesche, M., Althausen, D., Schladitz, A., Müller, D., Otto, S., Trautmann, T., Dinter, T., von Hoyningen-Huene, W., and Kahn, R.: Spectral surface albedo over Morocco and its impact on the radiative forcing of Saharan dust, Tellus, 61B, 252–269, 2009.

Chang, F.–L., Li, Z.: A Near-Global Climatology of Single-Layer and Overlapped Clouds and Their Optical Properties Retrieved from Terra/MODIS Data Using a New Algorithm, J. of Climate, 18, 4752–4771, 2005.

Eichler, H., Ehrlich, A., Wendisch, M., Mioche, G., Gayet, J.-F., Wirth, M., Emde, C., and Minikin, A.: Influence of ice crystal shape on retrieval of cirrus optical thickness and effective radius: A case study, J. Geophys. Res., 114, D19203, doi:doi:10.1029/2009JD012215, 2009.

Field, P. R., Wood, R., Brown, P. R. A., Kaye, P. H., Hirst, E., Greenaway, R., and Smith, J. A.: Ice particle interarrival times measured with a fast FSSP, J. Atmos. Oceanic Technol., 20, 249–261, 2003.

Field, P. R., Heymsfield, A., and Bansemer, A.: Shattering and particle interarrival times measured by Optical Array Probes in ice clouds, J. Atmos. Oceanic Technol., 23, 1357–1370, 2006.

Francis, P., Hignett, P., and Macke, A.: The retrieval of cirrus cloud properties from aircraft multi-spectral reflectance measurements during EUCREX '93, Quart. J. Roy. Meteor. Soc., 124, 1273–1291, 1998.

Frey, W., Eichler, H., de Reus, M., Maser, R., Wendisch, M., and Borrmann, S.: A new airborne tandem platform for collocated measurements of microphysical cloud and radiation properties, Atmos. Meas. Tech., 2, 147–158, 2009.

Gayet, J. F., Auriol, F., Minikin, A., Strom, J., Seifert, M., Krejci, R., Petzold, A., Febvre, G., and Schumann, U.: Quantitative measurement of the microphysical and optical properties of cirrus clouds with four different in situ probes: Evidence of small ice crystals, Geophys. Res. Lett., 29, 83-1 – 83-4, doi:10.1029/2001GL014 342, 2002.

Henrich, F., Siebert, H., Jäkel, E., Shaw, R. A., and Wendisch, M.: Collocated measurements of boundary-layer cloud microphysical and radiative properties and comparison with satellite retrievals, J. Geophys. Res., 115, D24 214, doi:10.1029/2010JD013930, 2010.

IPCC: Climate Change 2013: The Physical Science Basis, Cambridge University Press, Cambridge, United Kingdom and New York, NY, USA, 2013.

Keil, A. and Haywood, J. M.: Solar radiative forcing by biomass burning aerosol particles during SAFARI 2000: A case study based on measured aerosol and cloud properties, J. Geophys. Res., 108, 8467, doi:10.1029/2002JD002315, 2003.

Klingebiel, M., de Lozar, A., Molleker, S., Weigel, R., Roth, A., Schmidt, L., Meyer, J., A., E., Neuber, R., M., W., and Borrman, S.: Arctic low–level boundary layer clouds: in situ measurements and simulations of mono– and bimodal supercooled droplet size distributions at the top layer liquid phase cloud, Atm. Chem. Phys., 15, 617–631, 2015.

Korolev, A. V., Emery, E. F., Strapp, J. W., Cober, S. G., and Isaac, G. A.: Quantification of the Effects of Shattering on Airborne Ice Particle Measurements, J. Atmos. Ocean Technol., 30, 2527–2553, 2013.

Liou, K.-N.: Influence of cirrus clouds on weather and climate processes: A global perspective, Mon. Wea. Rev., 114, 1167–1199, 1986.

Lynch, K., Sassen, K., Starr, D., Stephens, G., Heymsfield, A., Liou, K.-N., Minnis, P., and Platt, C.: Cirrus, Oxford University Press, New York, 2002.

Mayer, B. and Kylling, A.: Technical note: The *libRadtran* software package for radiative transfer calculations - description and examples of use, Atmos. Chem. Phys., 5, 1855–1877, 2005.

McFarquhar, G. M., Um, J., Freer, M., Baumgardner, D., Kok, G. L., and Mace, G.: Importance of small ice crystals to cirrus properties: Observations from the Tropical Warm Pool International Cloud Experiment (TWP-ICE), Geophys. Res. Lett., 34, L13803, doi:10.1029/2007GL029865, 2007.

Müller, S., Hoor, P., Berkes, F., Bozem, H., Klingebiel, M., Reutter, P., Smit, H. G. J., Wendisch, M., Spichtinger, P., and Borrman, S.: In-situ detection of stratosphere-troposphere-exchange of cirrus particles in the mid-latitudes, Geophys. Res. Let., 42, doi:10.1002/2014GL062556, 2015.

Pilewskie, P. and Valero, F. P. J.: Radiative effects of the smoke clouds from the Kuwait oil fires, J. Geophys. Res., 97, 14 541–14 544, 1992.

Platt, C. M. R., Reynolds, D. W., and Abshire, N. L.: Satellite and Lidar Observations of the Albedo, Emittance and Optical Depth of Cirrus compared to Model Calculations , Monthly Weather Review, 108, 195–204, 1980.

Schlimme, I., Macke, A., and Reichardt, J.: The impact of ice crystal shapes, size distributions, and spatial structures of cirrus clouds on solar radiative fluxes, J. Atmos. Sci., 62, 2.274–2.283, 2005.

Sassen, K., and Comstock, J. M.: A Midlatitude Cirrus Cloud Climatology from the Facility for Atmospheric Remote Sensing. Part III: Radiative Properties, J. Atmos. Sci., 58, 2.113–2.127, 2001.

Stamnes, K., Tsay, S.-C., Wiscombe, W., and Laszlo, I.: DISORT, a General-Purpose Fortran Program for Discrete-Ordinate-Method Radiative Transfer in Scattering and Emitting Layered Media: Documentation of Methodology, Tech. rep., Dept. of Physics and Engineering Physics, Stevens Institute of Technology, Hoboken, NJ 07030, 2000.

Wendisch, M. and Brenguier, J.-L.: Airborne Measurements for Environmental Research – Methods and Instruments, Wiley–VCH Verlag GmbH & Co. KGaA, Weinheim, Germany, Weinheim, Germany, iSBN: 978-3-527-40996-9, 2013.

Wendisch, M., Müller, D., Schell, D., and Heintzenberg, J.: An airborne spectral albedometer with active horizontal stabilization, J. Atmos. Oceanic Technol., 18, 1856–1866, 2001.

Wendisch, M., Pilewskie, P., Pommier, J., Howard, S., Yang, P., Heymsfield, A. J., Schmitt, C. G., Baumgardner, D., and Mayer, B.: Impact of cirrus crystal shape on solar spectral irradiance: A case study for subtropical cirrus, J. Geophys. Res., 110, D03 202, doi:10.1029/2004JD005294, 2005.

Wendisch, M., Yang, P., and Pilewskie, P.: Effects of ice crystal habit on thermal infrared radiative properties and forcing of cirrus, J. Geophys. Res., 112, D03 202, doi:10.1029/2006JD007899, 2007.

Werner, F., Siebert, H., Pilewskie, P., Schmeissner, T., Shaw, R. A., and Wendisch, M.: New airborne retrieval approach for trade wind cumulus properties under overlying cirrus, J. Geophys. Res., 118, 3634–3649, doi:10.1002/jgrd.50334, http://dx.doi.org/10.1002/jgrd.50334, 2013.

Werner, F., Ditas, F., Siebert, H., Simmel, M., Wehner, B., Pilewskie, P., Schmeissner, T., Shaw, R. A., Hartmann, S., Wex, H., Roberts, G. C., and Wendisch, M.: Twomey effect observed from collocated microphysical and remote sensing measurements over shallow cumulus, J. Geophys. Res., 119, 1534–1545, doi:10.1002/2013JD020131, http://dx.doi.org/10.1002/2013JD020131, 2014.

Wylie, D., Menzel, W., Woolf, H., and Strabala, K.: Four years of global cirrus cloud statistics using HIRS, J. Climate, 7, 1972–1986, 1994.

Yang, P., Wei, H. L., Huang, H. L., Baum, B. A., Hu, Y. X., Kattawar, G. W., Mishchenko, M. I., and Fu, Q.: Scattering and absorption property database for nonspherical ice particles in the near- through far-infrared spectral region, Appl. Opt., 44, 5512–5523, 2005.

Yang, P., Bi, L., Baum, B. A., Liou, K. N., Kattawar, G. W., Mishchenko, M. I., and Cole, B.: Spectrall consistent scatterin, absorption, and polarization properties of atmospheric ice crystals at wavelengths from 0.2 to 100 μm, J. Atmos. Sci., 70, 330–347, 2013.

Zhang, Y., Macke, A., and Albers, F.: Effect of crystal size spectrum and crystal shape on stratiform cirrus radiative forcing, Atmos. Res., 52, 59–75, 1999.

Figure 1. Photo from the Learjet 35A with towed AIRcraft TOwed Sensor Shuttle. The picture was taken during a test flight from a second aircraft. The cable was artificially thickened to make it visible in the photo.

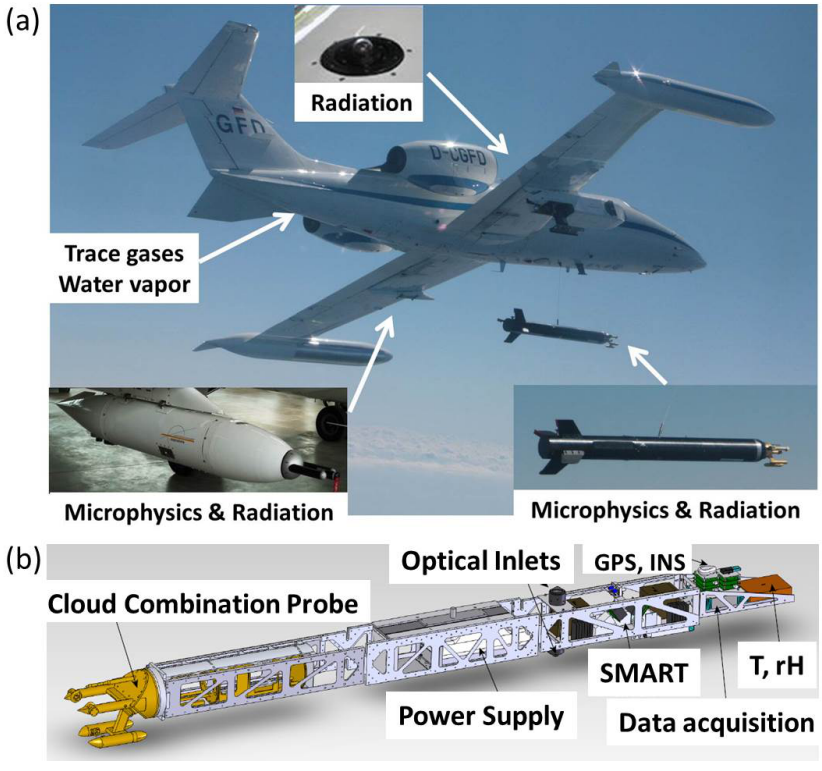

Figure 2. (a) Assembly of the research aircraft Learjet 35A, the towed AIRTOSS, and the wing pod containing instruments measuring radiation, microphysical parameter, water vapor, and trace gases. (b) Sketch of the AIRTOSS setup.

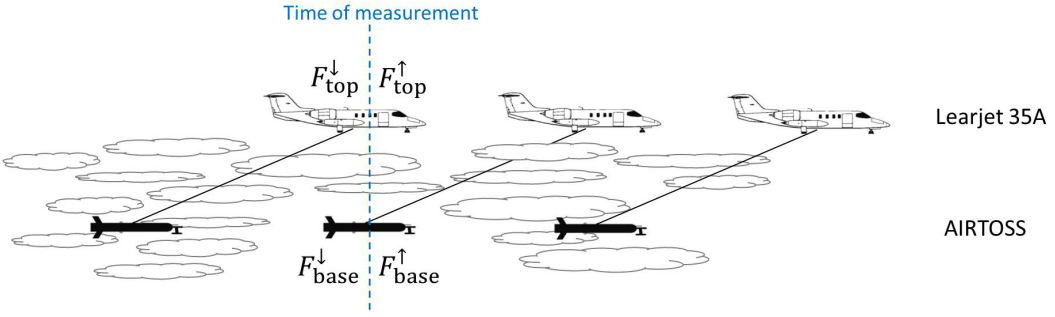

Figure 3. Schematic sketch of measurement setup to measure collocated upward ($F^{\uparrow}$) and downward ($F^{\downarrow}$) irradiance at two altitudes (base, top).

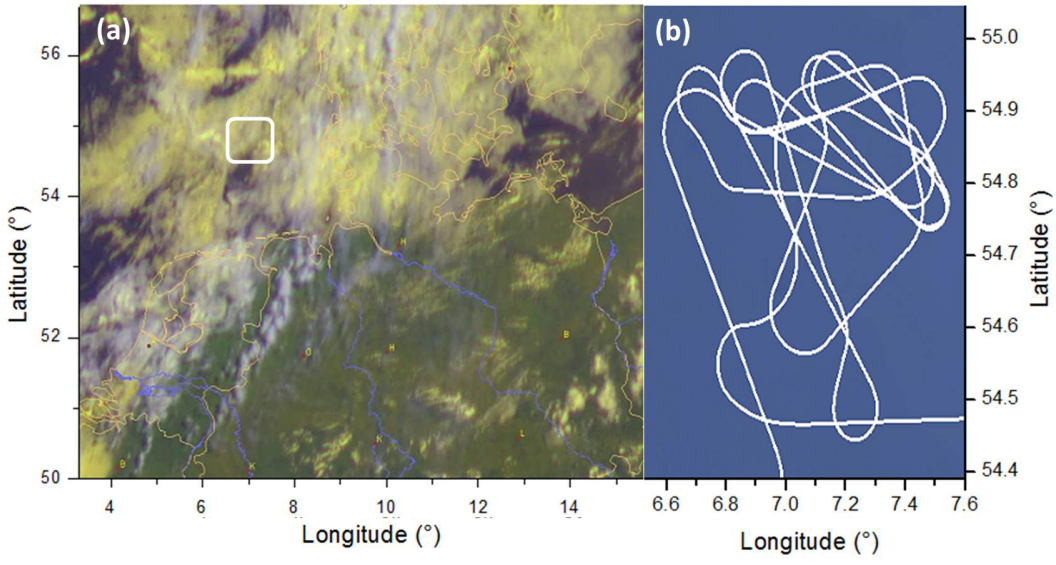

Figure 4. (a) Composite satellite image of the cloud situation on 30 August 2013 at 9:45 UTC showing high–level cirrus (white) above low–level water clouds (yellow, Deutscher Wetterdienst / EUMETSAT). In (b) the flight track of the measuring flight in the restricted area (white box in (a)) above the North Sea near the island of Helgoland, North Germany, is shown.

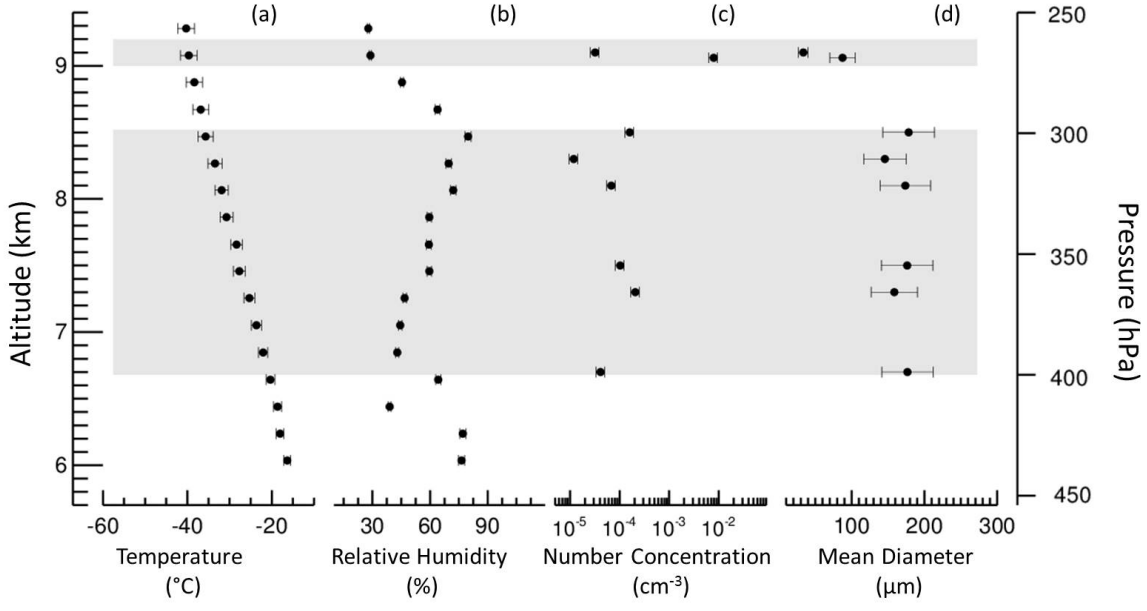

Figure 5. Vertical profiles of (a) temperature, (b) relative humidity, measured on the Learjet 35A, (c) number concentration, and (d) mean diameter, derived by CIPg on AIRTOSS, from the flight of 30 August 2013. The bars show the corresponding measurement uncertainties. The gray areas indicate the vertical extent of the cirrus layers.

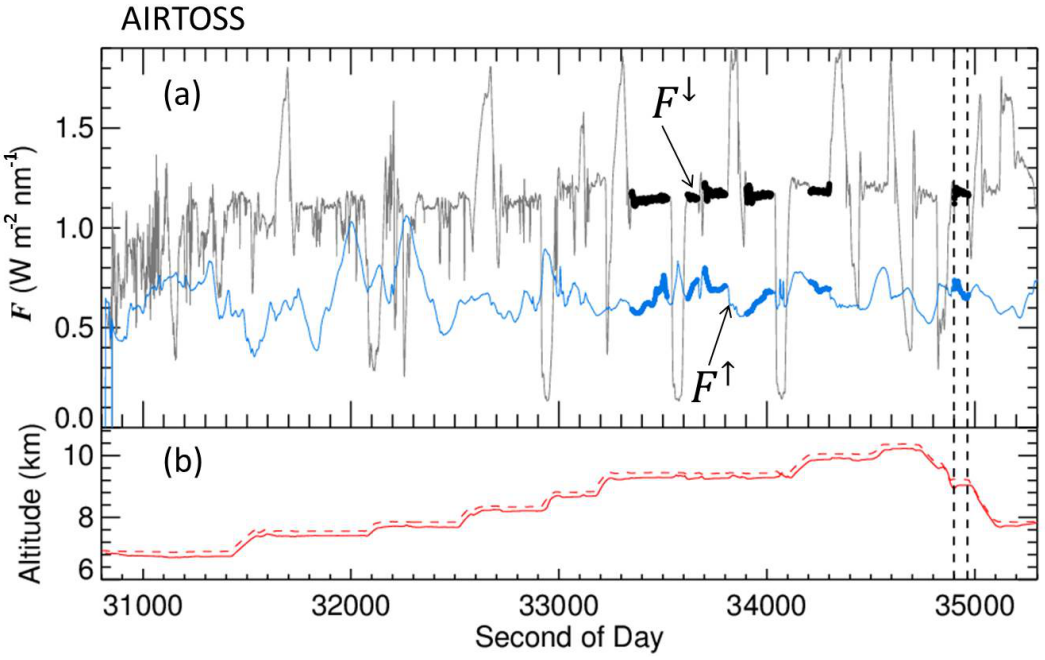

Figure 6. (a) Time series of downward (gray) and upward (light blue) irradiance F ($\mathrm{W\,m^{-2}\,nm^{-1}}$) measured on AIRTOSS at one wavelength (550 nm) from the flight of 30 August 2013. The thickened line periods mark the measuring points at straight flight legs. The red lines in (b) show the altitude of AIRTOSS (solid) and Learjet (dashed). The vertical dashed lines mark the period of the measurement example in Fig. 7.

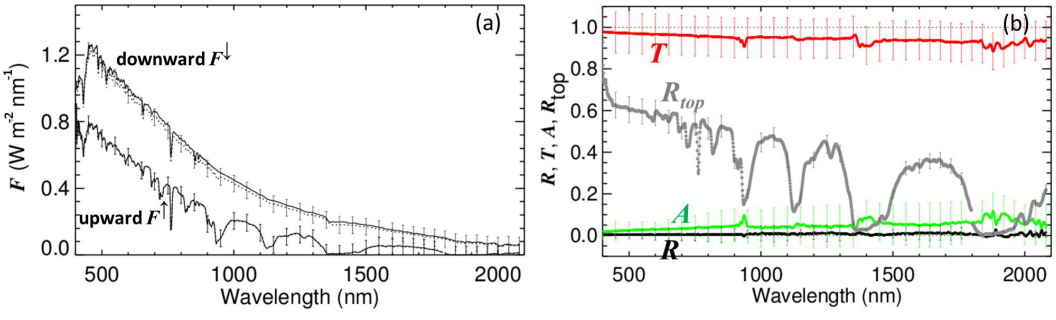

Figure 7. (a) The measured, averaged, spectral downward and upward irradiance F from the aircraft above the cloud layer (solid lines) and AIRTOSS below the cloud layer (dotted lines) at the time period, indicated by the vertical dashed lines in Fig. 6. $F^{\downarrow}_{\mathrm{top}}$ (solid line) is simulated. (b) shows spectral reflectivity (black), transmissivity (red), absorptivity (green), and cloud top albedo (gray) according to irradiance in (a). The vertical bars indicate the systematic errors due to measurement uncertainties.

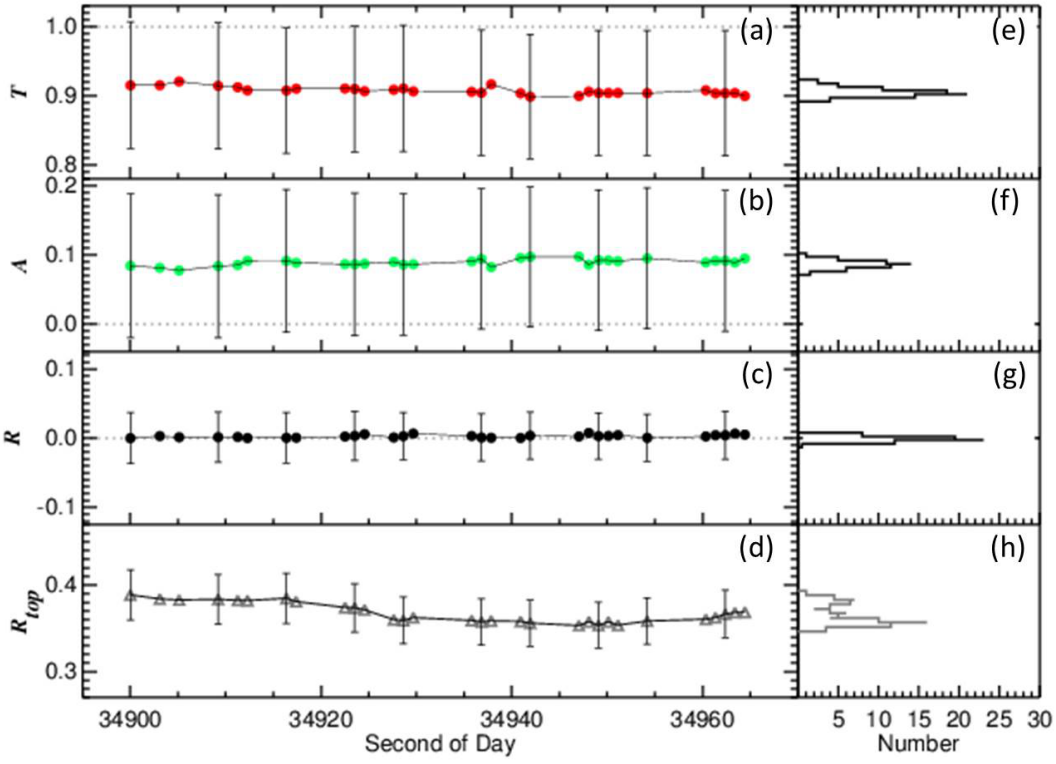

Figure 8. Time series of (a) transmissivity, (b) absorptivity, and (c) reflectivity (at 1640 nm) for the cirrus layer between 9.0 and 9.2 km altitude on 30 August 2013. The associated cloud top albedo is plotted in (d). The vertical bars represent the errors due to measurement uncertainties. (e) – (h) show the histograms, respectively.

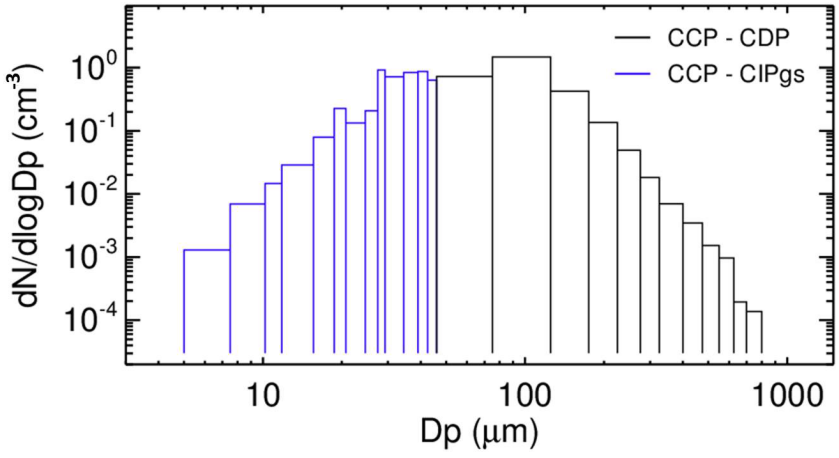

Figure 9. Number size distribution of a cirrus cloud, measured during the AIRTOSS campaign by the Cloud Combination Probe at the AIRcraft TOwed Sensor Shuttle.

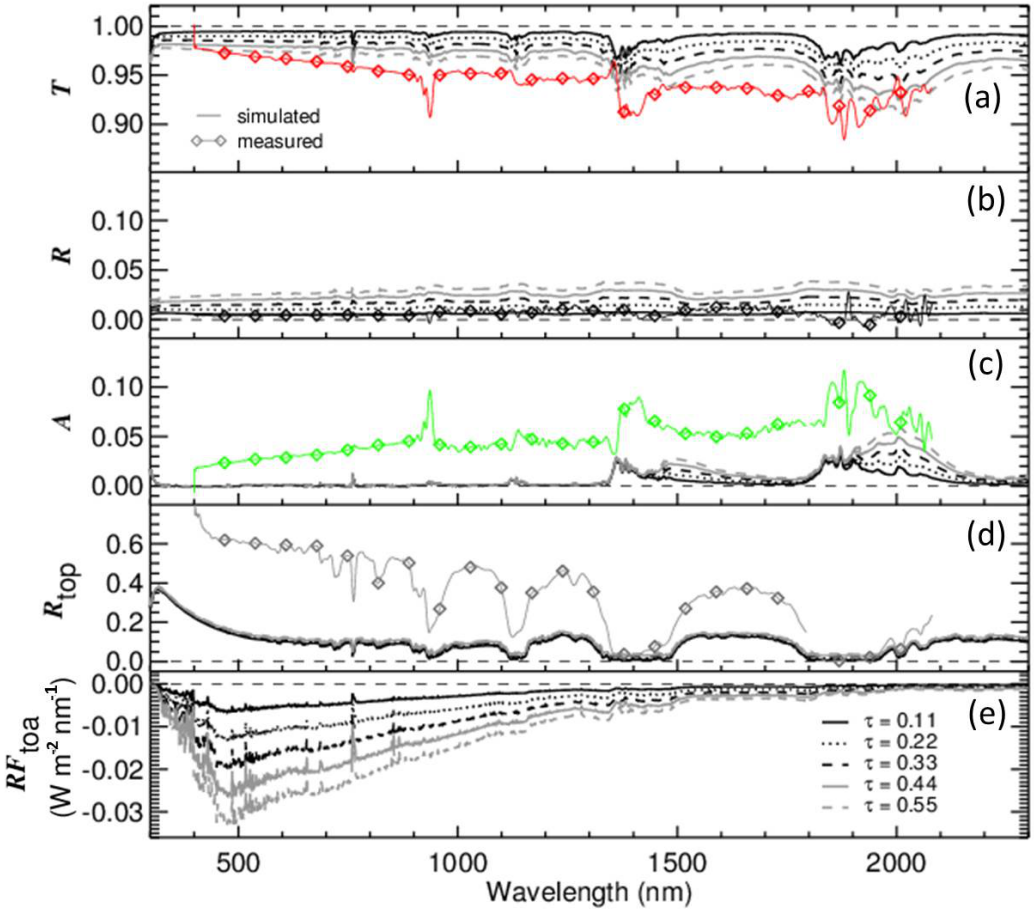

Figure 10. The lines show simulated, spectral (a) transmissivity, (b) reflectivity, and (c) absorptivity of a cirrus layer between 9 km and 9.2 km altitude. (e) are the radiative forcings at TOA, respectively. The simulations are based on a measured number size distribution assuming the mixture of shapes according Baum et al. (2005). Inserted is the measurement case (diamonds) from Fig.7.

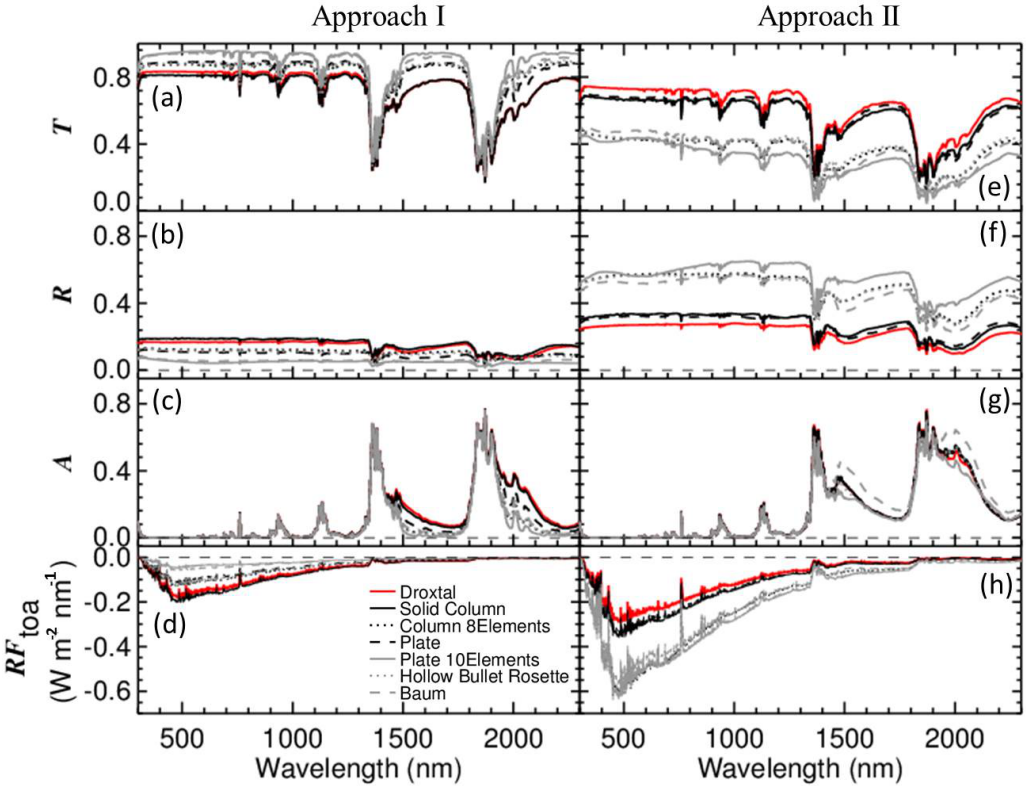

Figure 11. Spectral (a,e) transmissivity, (b,f) reflectivity, and (c,g) absorptivity of a cirrus layer between 6.7 and 8.5 km altitude. (e,h) are the radiative forcings at TOA, respectively. The simulations are based on a measured number size distribution assuming different ice particle shapes. The two panels indicate two conditions: constant number size distribution (Approach I) and constant ice water content (Approach II).

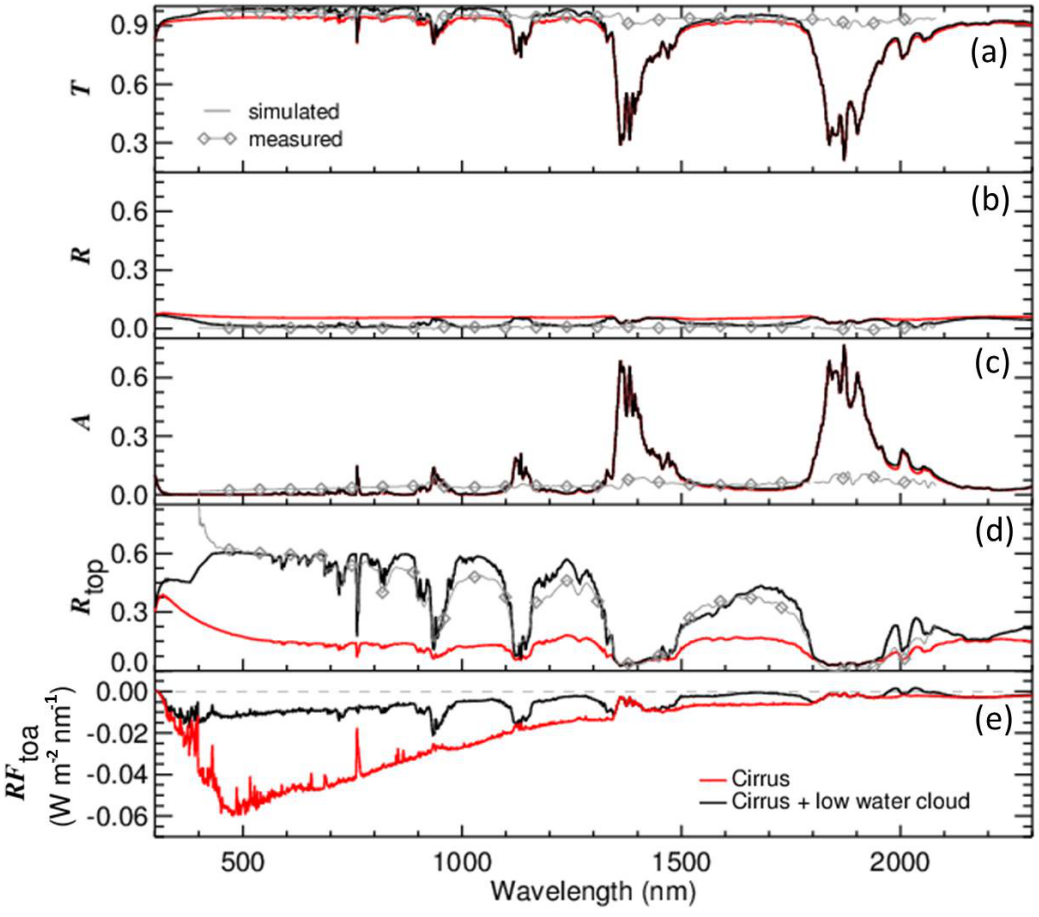

Figure 12. Same as Fig.10 assuming the mixture according to Baum et al. (2005) between 6.7 and 8.5 km altitude (τ_{Cirrus} = 1). An additional low water cloud with τ = 20 is included between 1.0 and 1.25 km altitude. Inserted is the measurement case (gray diamonds).

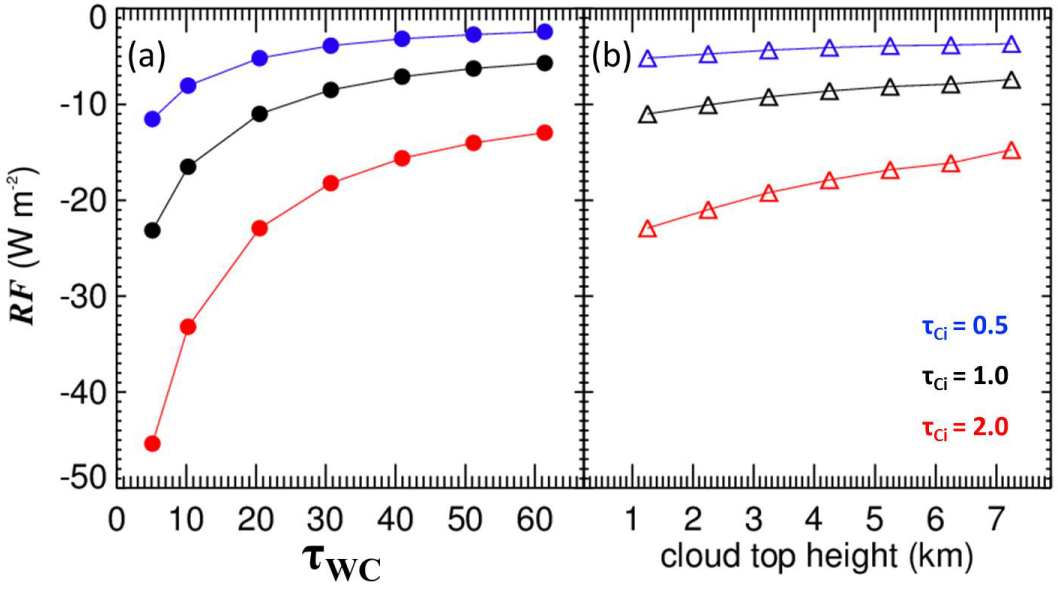

Figure 13. Integrated values of cirrus radiative forcing when a low water cloud is present. The optical thickness (left panel), and the top height (right panel) of the water cloud are varied. The colors indicate the different cirrus optical thicknesses.

Table 1. Optical thicknesses at λ=550 nm and effective radii (μm) for a cirrus between 6.7 km and 8.5 km altitude assuming different ice crystal shapes for Approach I (constant number size distribution) and Approach II (constant ice water content).

	Approach I		Approach II	
	τ	r_{eff}	τ	r_{eff}
Droxtal	1.49	88.5	2.68	76.5
Solid Column	1.50	88.5	3.20	56.1
Column 8 Elements	0.77	88.5	7.45	27.3
Plate	1.15	88.5	4.44	28.7
Plate 10 Elements	0.54	88.5	15.4	11.9
Hollow Bullet Rosette	0.97	88.5	9.52	17.2
Baum	1.00	88.5	5.09	23.8